




---

# SALT: INTRODUCING A FRAMEWORK FOR HIERARCHICAL SEGMENTATIONS IN MEDICAL IMAGING USING SOFTMAX FOR ARBITRARY LABEL TREES

---

Sven Koitka <sup>1,2,\*</sup>  Giulia Baldini <sup>1,2,\*</sup>  Cynthia S. Schmidt <sup>2,3</sup>  Olivia B. Pollok <sup>2</sup> Obioma Pelka <sup>2</sup>

Judith Kohnke <sup>1,2</sup> Katarzyna Borys <sup>1,2</sup>  Christoph M. Friedrich <sup>4,5</sup>  Benedikt M. Schaarschmidt <sup>1</sup> 

Michael Forsting <sup>1</sup> Lale Umutlu <sup>1</sup> Johannes Haubold <sup>1,2</sup>  Felix Nensa <sup>1,2</sup>  René Hosch <sup>1,2,†</sup> 

## ABSTRACT

### Background:

Traditional segmentation networks approach anatomical structures as standalone elements, overlooking the intrinsic hierarchical connections among them. This study introduces Softmax for Arbitrary Label Trees (SALT), a novel approach designed to leverage the hierarchical relationships between labels, improving the efficiency and interpretability of the segmentations.

### Materials and Methods:

This study introduces a novel segmentation technique for CT imaging, which leverages conditional probabilities to map the hierarchical structure of anatomical landmarks, such as the spine's division into lumbar, thoracic, and cervical regions and further into individual vertebrae. The model was developed using the SAROS dataset from The Cancer Imaging Archive (TCIA), comprising 900 body region segmentations from 883 patients. The dataset was further enhanced by generating additional segmentations with the TotalSegmentator, for a total of 113 labels. The model was trained on 600 scans, while validation and testing were conducted on 150 CT scans. Performance was assessed using the Dice score across various datasets, including SAROS, CT-ORG, FLARE22, LCTSC, LUNA16, and WORD. Additionally, 95% confidence intervals (CI) were computed using 1000 rounds of bootstrapping.

### Results:

Among the evaluated datasets, SALT achieved its best results on the LUNA16 and SAROS datasets, with Dice scores of 0.93 (95% CI: 0.919, 0.938) and 0.929 (95% CI: 0.924, 0.933) respectively. Additionally, the model demonstrated reliable accuracy across other datasets, scoring 0.891 (95% CI: 0.869, 0.906) on CT-ORG and 0.849 (95% CI: 0.844, 0.854) on FLARE22. Moreover, the LCTSC dataset showed a score of 0.908 (95% CI: 0.902, 0.914) and the WORD dataset also showed good performance with a score of 0.844 (95% CI: 0.839, 0.85). Furthermore, SALT is capable of segmenting a whole-body CT with 1000 slices in an average of 35 seconds.

### Conclusion:

SALT used the hierarchical structures inherent in the human body to achieve whole-body segmentations with an average of 35 seconds per CT scan. This rapid processing underscores its potential for integration into clinical workflows, facilitating the automatic and efficient computation of full-body segmentations with each CT scan, thus enhancing diagnostic processes and patient care.

---

<sup>1</sup>Institute of Interventional and Diagnostic Radiology and Neuroradiology, University Hospital Essen, Essen, Germany

<sup>2</sup>Institute for Artificial Intelligence in Medicine (IKIM), University Hospital Essen, Essen, Germany

<sup>3</sup>Institute for Transfusion Medicine, University Hospital Essen, Essen, Germany

<sup>4</sup>Institute for Medical Informatics, Biometry and Epidemiology (IMIBE), University Hospital Essen, Essen, Germany

<sup>5</sup>Faculty of Computer Science, University of Applied Sciences and Arts, Dortmund, Germany

\*Sven Koitka and Giulia Baldini contributed equally

†Corresponding author: Rene.Hosch@uk-essen.de

## 1 Introduction

Computed Tomography (CT) imaging stands out as one of the most comprehensive [13, 20, 36, 41] tools in the field of diagnostic imaging, with the number of CT scans increasing by 4% per year worldwide [48]. With the rising volume of CT scans, radiologists also face a growing workload, highlighting the importance of adopting automated solutions for support. Moreover, CT scans contain a substantial volume of information, and only a portion is used for specific diagnosis purposes. A substantial amount of potentially clinically valuable information remains unexploited and is the focus of current research [6, 18, 53]. In this context, deep learning networks have the capability of automating tasks and extracting information from scans with little additional cost besides algorithm training. In particular, automated segmentation of CT scans is now a widespread technique for identifying key anatomical features such as organs, tissues, and vessels [26, 43, 53]. These detailed segmentations aid radiologists in making accurate diagnoses [3] and have been linked to indicators of a patient’s well-being [1, 19]. This capability enables automated quantification of segmentations, with metrics such as organ volumetries gaining recognition for their role in predicting overall survival outcomes [17, 22]. Furthermore, CT scans enable the automated calculation of Body Composition Analysis (BCA), which quantifies the amount of fat, muscle, and bone [14, 27, 38, 39] and is proving to be valuable in monitoring disease progression [19, 23, 33] and predicting patient survival outcomes [15, 21].

The currently existing models for full-body segmentation, such as TotalSegmentator [16, 53], often rely on multiple models for segmenting CT scans when the number of labels becomes too extensive for a single model to handle efficiently. Additionally, completing a full segmentation can take several minutes, which is impractical for scenarios where a segmentation algorithm is expected to constantly operate in the background as part of a hospital’s data acquisition process.

In response to this problem, we introduce the Softmax for Arbitrary Label Trees (SALT) framework, an approach that employs a single, robust model to efficiently manage a broad spectrum of labels. The SALT framework harnesses hierarchical relationships to segment a vast range of anatomical landmarks, reflecting the natural tree-like organization of the human anatomy. By employing conditional probabilities, this framework models the intricate relationships between these landmarks, capturing the complex network of connections among various anatomical structures. In this study, an application of the SALT framework to 3-dimensional CT scans using a nnUNet [16] architecture is presented. However, the flexibility of this framework allows for its adaptation to other contexts, accommodating both 2D and 3D imaging across diverse image types, and could be used with a wide range of deep learning algorithms. This adaptability underscores the SALT framework’s potential as a universal tool for medical image analysis. This optimization aims to resolve existing bottlenecks and substantially improve the utility of CT scan data in real-time clinical settings, facilitating the seamless operation of the segmentation algorithm within the hospital’s data acquisition process.

## 2 Materials and Methods

### 2.1 Datasets

This study used a selection of datasets available on The Cancer Imaging Archive (TCIA) [9] to train and evaluate the SALT approach. For the training, 750 CT scans from the Sparsely Annotated Region and Organ Segmentation (SAROS) [9, 25] dataset were used (600 for training and 150 for validation). In this dataset, the segmentations target anatomical landmarks that are relevant for body composition analysis (BCA) [14, 27]. The annotations cover a wide range of areas such as the abdominal and thoracic cavities, bones, brain, mediastinum, muscles, pericardium, spinal cord, and subcutaneous tissue. In addition to these annotations, segmentations of organs, vessels, and specific muscles and bones were generated using Version 1 of the TotalSegmentator models [16, 52, 53] for the same dataset of 750 scans. The TotalSegmentator predictions were then fused with the SAROS annotations to create a single dataset of 750 scans containing all labels. For SAROS, smaller labels such as the thyroid, submandibular, and parotid glands were not included in the final segmentation. The SAROS segmentations encompass larger and more general areas, so the TotalSegmentator predictions were superimposed on the SAROS labels, as a subclassification of larger areas. This fusion is illustrated in Figure 1, which highlights the natural tree-like organization of the human body. For example, the body encompasses the thoracic cavity, which itself includes organs like the lungs and heart. These organs, in turn, can be subdivided further into more specific segments, such as the lobes of the lungs and the atria and ventricles of the heart.

For the evaluation, an additional independent test set of 150 CT scans from SAROS and other publicly available datasets were used: CT Volumes with Multiple Organ Segmentations (CT-ORG) [5, 9, 44] Fast and Low-resource Semi-supervised Abdominal Organ Segmentation (FLARE22) [31, 32], Lung CT Segmentation Challenge (LCTSC) [9, 54, 55], Lung Nodule Analysis 2016 (LUNA16) [2, 50], and Whole Abdominal Organ Dataset (WORD) [30]. However, the “gallbladder” label from the WORD dataset was omitted because the masks were either very few points and not an

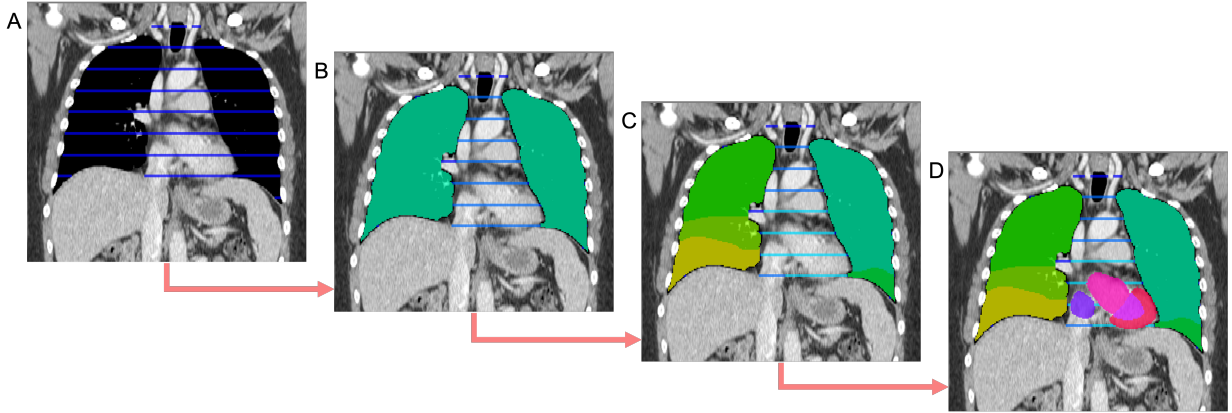


Figure 1: **Example of a hierarchical segmentation.** A) In the thorax, the biggest region is the thoracic cavity. B) The thoracic cavity can then be subdivided into lungs and mediastinum. C) The mediastinum has a further subregion the pericardium, and the lungs can be subdivided into lower/middle/upper left/right lobes. D) The pericardium contains the heart, which can be subdivided into myocardium and left/right ventricle/atrium. The full segmentations originate from the TotalSegmentator, while the sparse segmentations are from SAROS.

actual segmentation, a segmentation of the common bile duct, or they were segmentations of a tumor (see Figure 8 of Appendix A). The final composition of the evaluation dataset, together with the number of cases and the used labels, is reported in Table 1.

### 2.1.1 Dataset Postprocessing

The labels from all datasets underwent postprocessing to ensure the hierarchical structure by either merging or splitting the original segmentations. An example of merging is the lung label, which was not present in the TotalSegmentator labels but could be inferred by merging the upper, lower, middle left, and right lobes. In some cases, splitting was necessary to ensure the tree structure, as each label can only have one parent. For instance, the aorta passes through the mediastinum, pericardium, and abdominal cavity, which would imply three parents. To preserve the tree structure, the aorta label was split into three separate regions: “aorta thoracica pass pericardium”, “aorta thoracica pass mediastinum”, and “aorta abdominalis”. Similar splitting was performed for the inferior vena cava and pulmonary artery. Furthermore,

Table 1: **Datasets used for the evaluation.** Multiple datasets from TCIA were used for evaluating SALT: CT Volumes with Multiple Organ Segmentations (CT-ORG), Fast and Low-resource Semi-supervised Abdominal Organ Segmentation (FLARE22), Lung CT Segmentation Challenge (LCTSC), Lung Nodule Analysis 2016 (LUNA16), Sparsely Annotated Region and Organ Segmentation (SAROS), and Whole Abdominal Organ Dataset (WORD). For SAROS, an independent test set was used for the evaluation. For each dataset, the number of included CT scans and the labels used for evaluation are reported.

Dataset	Number of Scans	Labels
CT-ORG [5, 9, 44]	21	Liver, bladder, lungs, kidneys, bone, brain.
FLARE22 [31, 32]	50	Liver, right kidney, spleen, pancreas, aorta, inferior vena cava, right adrenal gland, left adrenal gland, gallbladder, stomach, duodenum, left kidney.
LCTSC [9, 54, 55]	60	Spinal cord, lung right, lung left, heart.
LUNA16 [2, 50]	51	Upper right lobe, middle right lobe, lower right lobe, upper left lobe, lower left lobe.
SAROS [9, 24, 25]	150	Subcutaneous tissue, muscles, abdominal cavity, thoracic cavity, bones, mediastinum, pericardium, brain, spinal cord.
WORD [30]	140	Liver, spleen, kidney left, kidney right, stomach, pancreas, duodenum, colon, intestine, adrenal glands, bladder.

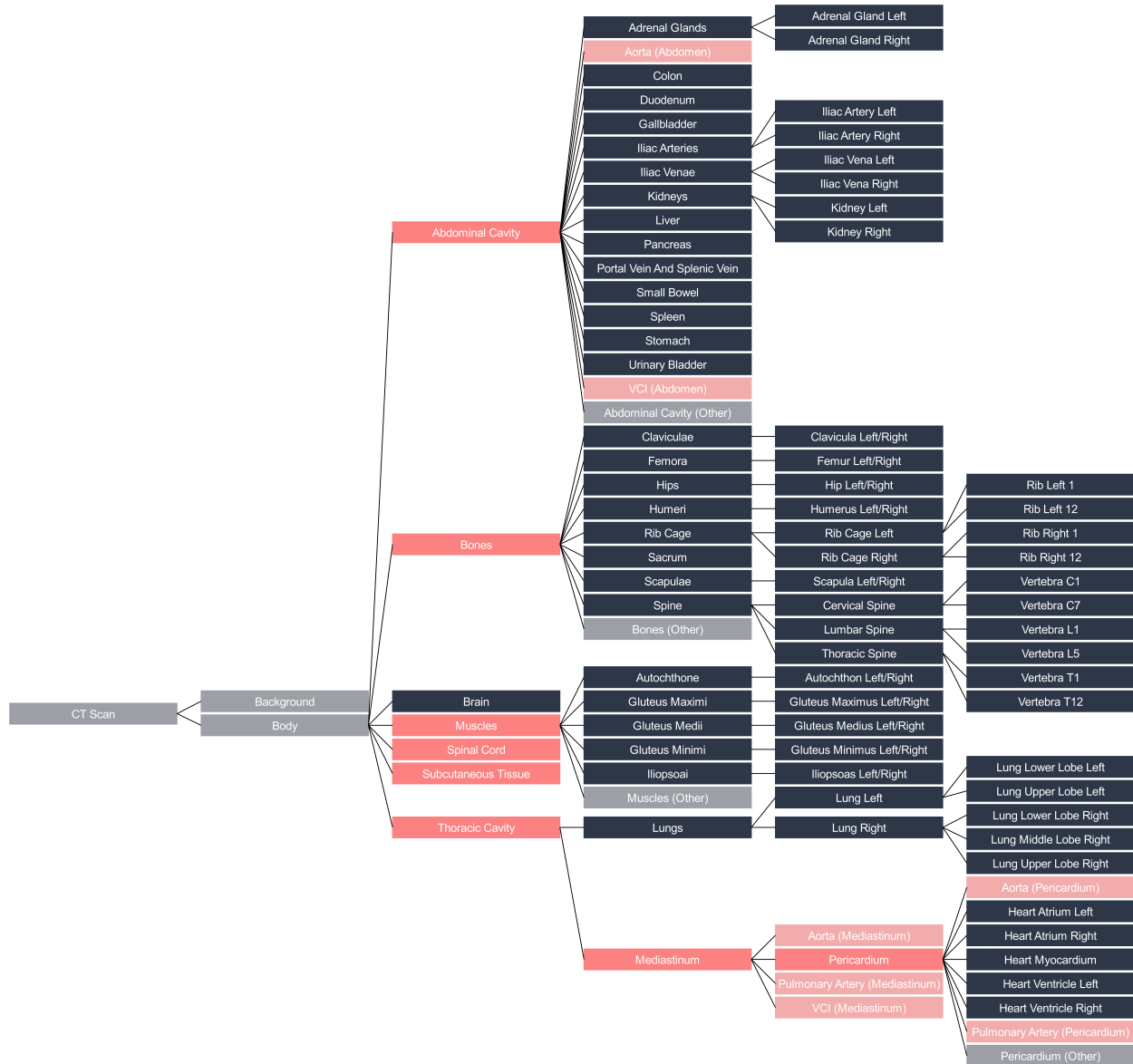


Figure 2: **Hierarchical labeling for the segmentation of anatomical landmarks.** The blue labels were generated with the TotalSegmentator, while the pink labels come from the SAROS dataset. The gray labels were also generated: “body” is the sum of all annotated voxels, while “background” is all non-annotated voxels. The “other” classes were created as the parts of the parents which were not annotated. The light pink labels were generated by splitting an existing TotalSegmentator label. Some vertebrae and ribs have been removed from this visualization for a better overview. For some bones and muscles with only left and right children, the two nodes were fused for better visualization.

in cases where the child labels were insufficient to fully annotate the volume of the parent label, additional labels were created. For instance, the thoracic cavity has two child labels, namely the lungs and the mediastinum (as depicted in Figure 1). However, these two volumes alone do not encompass the entire thoracic cavity. Therefore, an additional label (called “other”) was introduced to incorporate the remaining voxels and ensure a correct learning process for the model. After postprocessing, there were a total of 145 labels (excluding the root) and 113 leaf nodes. The hierarchical structure of the labels can be viewed in Figure 2.

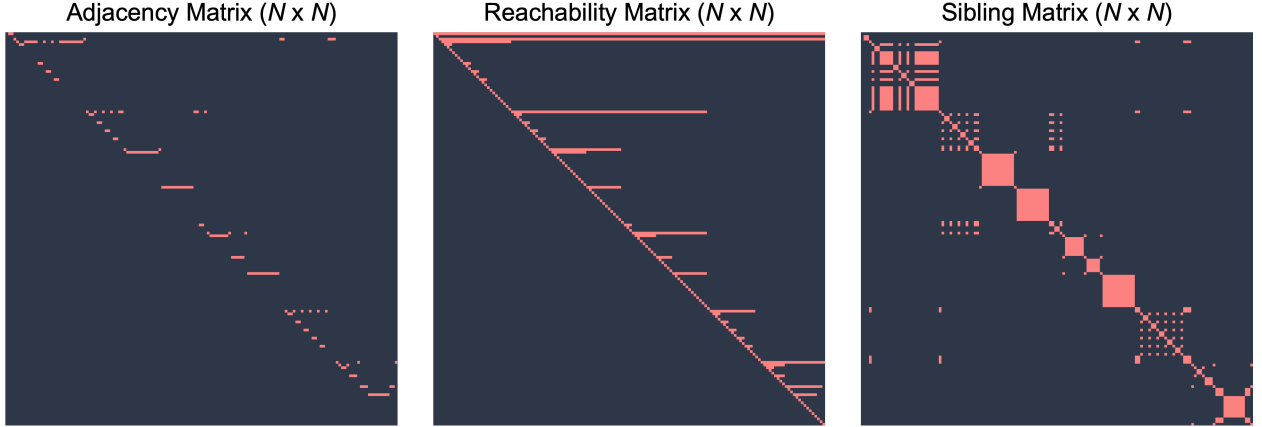


Figure 3: **Different representations of the tree class hierarchy.** From left to right: (1) The adjacency matrix encodes directed edges from parent to child nodes. (2) The reachability matrix encodes all nodes in the path from the root node to a specific node. (3) The sibling matrix encodes all sibling nodes for a specific node.

## 2.2 Modeling Conditional Probabilities for Trees

As visible from Figure 2, the hierarchical labels can be represented as an unweighted tree. An arbitrary tree can be defined by its adjacency matrix  $A$  of size  $N \times N$ , where  $N$  is the number of nodes and each value  $a_{i,j}$  of the matrix represents an edge between parent node  $i$  and child node  $j$ . Since the tree is unweighted,  $A$  has only binary elements [8], and  $a_{i,j} = 1$  represents a connection between parent node  $i$  and child node  $j$ .

Another useful structure is the reachability matrix  $R$ , which encodes in row  $i$  all the nodes  $j$  that can be reached from node  $i$ , and in column  $j$  all the traversed nodes between the root and node  $j$ . This matrix is also binary and it can be derived from the adjacency matrix using matrix multiplications and additions:

$$R = \sum_{v=0}^H A^v = A^0 + A^1 + \dots + A^H,$$

where  $H$  is the height of the arbitrary tree. Each power  $A^v$  represents the nodes that can be reached from any node with a path of size  $v$ , so the matrix  $A^{H+1}$  will be a zero matrix, as no two nodes have a distance that is larger than  $H$ . Another component is the sibling matrix  $S$ , which is also binary and encodes all local neighbors on the same level:

$$S = A^T \times A$$

An example for all three matrices,  $A$ ,  $R$ , and  $S$ , based on the employed dataset and the associated label structure is shown in Figure 3.

Using these matrices, the assignment of a voxel of the body to a specific class can be represented through conditional probabilities based on the tree structure. For instance, the probability of a voxel to belong to the right lower lobe of the lung depends on the probabilities of it belonging to the right lung, the lungs as a whole, the thoracic cavity, and the body. This concept is analogous to the one of Bayesian networks [46], which are acyclic directed graphs where each node contains probability information, and edges represent a direct influence between the nodes. In a Bayesian network, all relationships are expressed using conditional probabilities and can be simplified using the chain rule [46]. This can also be applied to our hierarchical tree, but a normalization step needs to be added to ensure that each node represents a probability. This can be done using a softmax function [7], which is commonly employed as an activation function in neural networks for multi-class classification tasks. Its outputs are probabilities that indicate the likelihood of the input being assigned to each class, and its sum is 1, just like for probabilities.

These concepts can be used to build a deep learning model that uses conditional probabilities and the softmax function as activation layer for segmentation. The model takes an input and outputs a feature map  $x$  with  $N$  channels, which is the number of nodes of the hierarchical tree. To enforce the hierarchical relationships, a final probability function for each class  $c$  can serve as the activation layer.

The probability  $P(y = c|x)$  that the final class  $y$  corresponds to class  $c|x$  can be computed using the chain rule as the product of the probabilities from the root node to node 40. The probability of each node is normalized using the softmax

for each sibling group, obtaining the following formula:

$$\begin{aligned} P(y = c|x) &= \prod_{i=1}^{R_c} P(y = i|x \bigcap_{j=1}^{i-1} y = j) \\ &= \prod_{i \in R_c} \frac{e^{-x_i}}{\sum_{k \in S_i} e^{-x_k}}, \end{aligned}$$

Here,  $R_c$  denotes the column  $c$  of  $R$ , which contains the nodes in the path between the root node and node  $c$ .  $S_i$  represents the siblings of node  $i$ , and  $x_i$  and  $x_j$  respectively correspond to the feature maps associated with node  $i$  and  $j$ . The resulting probabilities of all leaf nodes sum up to one, analogously to the softmax function. To illustrate an example of the probability chain, consider the process of determining the likelihood that a voxel is part of the left hip bone. This requires a sequential evaluation of the voxel’s probability of being within the body, within the bone, then associated with hip bones, and finally identified as part of the specific left hip bone, which can be expressed as:

$$\begin{aligned} P(y = \text{hip left}|x) &= P(y = \text{body}) \\ &\cdot P(y = \text{bones}|x \cap y = \text{body}) \\ &\cdot P(y = \text{hip}|x \cap y = \text{body} \cap y = \text{bones}) \\ &\cdot P(y = \text{hip left}|x \cap y = \text{body} \cap y = \text{bones} \cap y = \text{hip}). \end{aligned}$$

### 2.3 Model Preprocessing and Training

The SALT architecture in this paper consists of a DynUNet from the MONAI framework [10] (version 1.1, PyTorch [42] version 1.14), which is a reimplementation of the architecture utilized by nnUNet [16]. The output feature map of the DynUNet model has as many channels as there are nodes in the hierarchical tree. Due to SALT’s flexibility, the DynUNet could be substituted by any other model. The previously described probability functions were used to create an activation layer, which was used to generate the final probabilities, as illustrated in Figure 4.

Initially, all CT scans underwent several pre-processing steps: Left-Posterior-Inferior voxel reorientation, resampling to a voxel spacing of 1.5x1.5x1.5 mm, normalization of intensity values within the Hounsfield Units to scale the range from -1024 to 1024 to between 0 and 1, and random crops of size 192x192x48. The model was trained for 1000 epochs with 600 CT scans for training and 150 for validation. The AdamW optimizer [28] was used with an initial learning rate of 0.00025 and a weight decay of 0.00005. The learning rate was reduced during training using a cosine function [29].

The model used a hybrid loss based on categorical cross-entropy loss [35] and Dice loss [34], which are commonly used for medical segmentation tasks [16]. In contrast to the common use of these losses, SALT optimizes multiple classes at the same time by constructing an encoding of the nodes using the reachability matrix. Let  $R$  be the reachability matrix of size  $(N, N)$ , where  $N$  is the number of nodes in the tree, and let  $y$  be the ground truth label with  $|V|$  elements (each corresponding to a voxel’s label). We construct a new label  $y'$  of size  $(|V|, N)$  by indexing the reachability matrix  $R$  using the ground truth  $y$ . This operation maps each voxel label to its corresponding encoding column in  $R$ , or in other words,  $y'$  corresponds to the traversed nodes from the root to the voxel’s label. Considering the prediction  $\hat{y}$  of size  $(|V|, N)$ , the cross-entropy and the Dice loss can be computed using  $y'$  and  $\hat{y}$ . Unlike the conventional softmax approach, this method optimizes each node along with all its ancestors, which is a result of the label encoding and the implementation of chained conditional probabilities within the activation layers.

For the calculation of the evaluation metrics during training, a similar approach that uses the tree structure to encode each node was used. Technical details about this method are presented in Appendix C. Furthermore, the trained model and the code are available for review on GitHub under the following link: <https://github.com/UMEssen/SALT>.

### 2.4 Evaluation

The model’s performance was assessed with the Dice score [11] and with the normalized surface Dice score (NSD) [37]. The NSD measures the frequency at which the surface distance between volumes is under 3 mm, a metric previously employed by TotalSegmentator [53]. For a better comparison with existing models, the same metrics were also utilized to evaluate the predictions from Version 2 of the TotalSegmentator [16, 53] on the datasets from Table 1. Additionally, 95% confidence intervals (reported in square brackets) were computed by bootstrapping the scores of the evaluated CT scans. The bootstrapping was performed with 1000 iterations and the 2.5 and the 97.5 percentiles were utilized as upper and lower bound of the confidence intervals. To evaluate the variations in scores across datasets, the distributions of the Dice and NSD scores were compared for datasets that share the same organ labels.

For a better comparison, the evaluation datasets were also used to generate predictions from Version 2 of the TotalSegmentator [16, 53] and the same evaluation scores were computed. Moreover, the speed of the model was

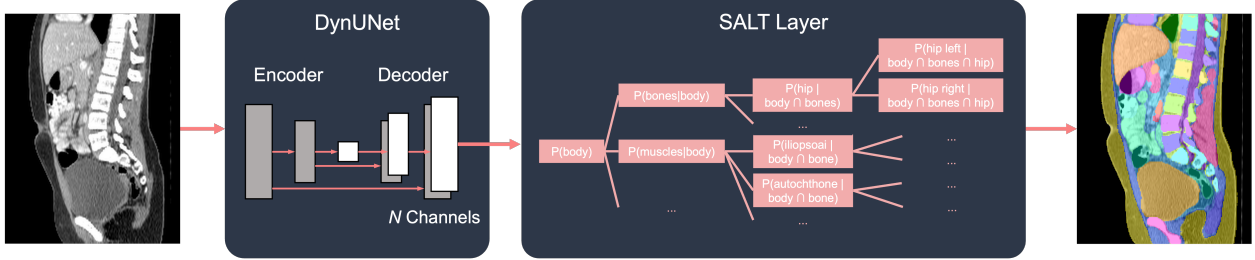


Figure 4: **Overview of the SALT architecture.** A DynUNet model is used to output feature maps containing  $N$  channels, where  $N$  is the number of nodes of the tree. The SALT layer builds conditional probabilities from the nodes of the tree and can be used analogously to a softmax function to create a segmentation.

evaluated in comparison with Version 1 and Version 2 of the TotalSegmentator and across multiple speed settings. For TotalSegmentator Version 1, tests were carried out on models with isotropic spacings of 1.5mm and 3mm. In the case of Version 2, models with isotropic spacings of 1.5mm, 3mm, and 6mm were examined. All experiments were performed by running the models on a single NVIDIA RTX A6000 card [40].

### 3 Results

#### 3.1 Segmentation Evaluation

The trained model showed a Dice of 0.891 [0.887, 0.896] and an NSD of 0.931 [0.927, 0.936]. An overall score for the different datasets is presented in Table 2 together with the scores obtained by Version 2 of the TotalSegmentator. The Dice scores and the NSD scores for the datasets are reported in Table 3, Table 4, Table 5, Table 6, Table 7 and Table 8 of Appendix B. Notably, the lungs, the liver, the spleen, and the stomach achieved the best scores across the different datasets.

Additionally, an evaluation of the speed of the model at inference time was also performed, which can be reviewed in Table 9. It is relevant to make a distinction between the inference time (the time the model takes to make a prediction) and the total time, as a large portion of the inference time is just spent postprocessing and storing the result. In Figure 5, a comparative analysis of SALT’s speed against both Version 1 and Version 2 of the TotalSegmentator is presented. This comparison clearly demonstrates that SALT consistently outperforms its counterparts, showing a notable speed advantage, especially with larger CT scans. Additionally, a speed comparison was conducted between SALT and the faster variants of TotalSegmentator that utilize lower spacing, with the findings detailed in Figure 9 of Appendix A. These “fast” alternatives of TotalSegmentator, which use a single model instead of five, also exhibit better speed. In these comparisons, the 3mm model from Version 2 of TotalSegmentator was consistently slower than or comparable to SALT. However, for larger images, the 3mm model of Version 1 and the 6mm model of Version 2 were faster.

Furthermore, the inner workings of the model can be better understood by examining the conditional probabilities used at various stages. As an example, the process of predicting the vertebra L4 is illustrated in Figure 6. This visualization effectively demonstrates how the model relies on these conditional probabilities to formulate its predictions.

Table 2: **Summary results of the model’s performance for the datasets.** The evaluation is performed in terms of Dice and Normalized Surface Dice (NSD) for both SALT and Version 2 of the TotalSegmentator (TSV2). The 95% confidence intervals were computed using 1000 rounds of bootstrapping, and the interval is reported in square brackets.

Metric	CT-ORG	FLARE22	LCTSC	LUNA16	SAROS	WORD
SALT (Dice)	0.891 [0.869, 0.906]	0.849 [0.844, 0.854]	0.908 [0.902, 0.914]	0.93 [0.919, 0.938]	0.929 [0.924, 0.933]	0.844 [0.839, 0.85]
TSV2 (Dice)	0.917 [0.898, 0.931]	0.892 [0.888, 0.897]	0.937 [0.931, 0.942]	0.952 [0.943, 0.959]	0.852 [0.846, 0.857]	0.84 [0.834, 0.846]
SALT (NSD)	0.884 [0.863, 0.905]	0.947 [0.942, 0.952]	0.886 [0.872, 0.899]	0.908 [0.89, 0.92]	0.98 [0.975, 0.984]	0.909 [0.903, 0.915]
TSV2 (NSD)	0.916 [0.895, 0.933]	0.954 [0.949, 0.959]	0.945 [0.935, 0.954]	0.934 [0.925, 0.943]	0.955 [0.949, 0.959]	0.906 [0.899, 0.912]

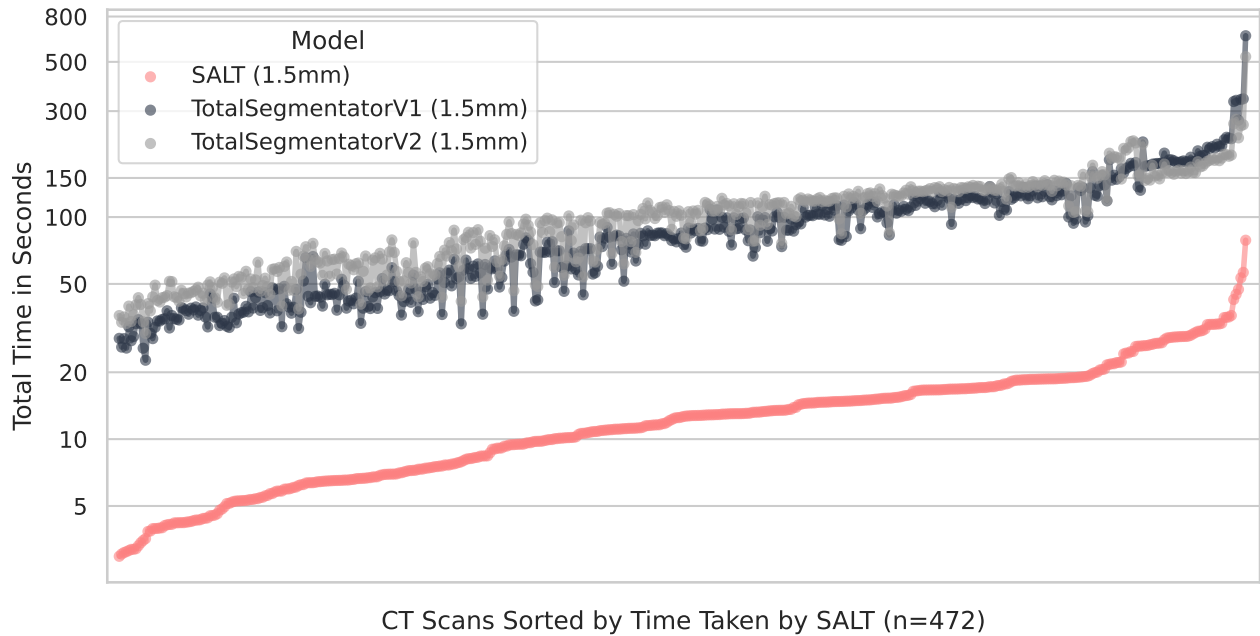


Figure 5: **Comparison between the speed of SALT and the TotalSegmentator.** Version 1 and 2 of the TotalSegmentator were run on the same set of 472 CT scans from Table 1. The TotalSegmentator models and SALT were trained on 1.5mm isotropic spacing.

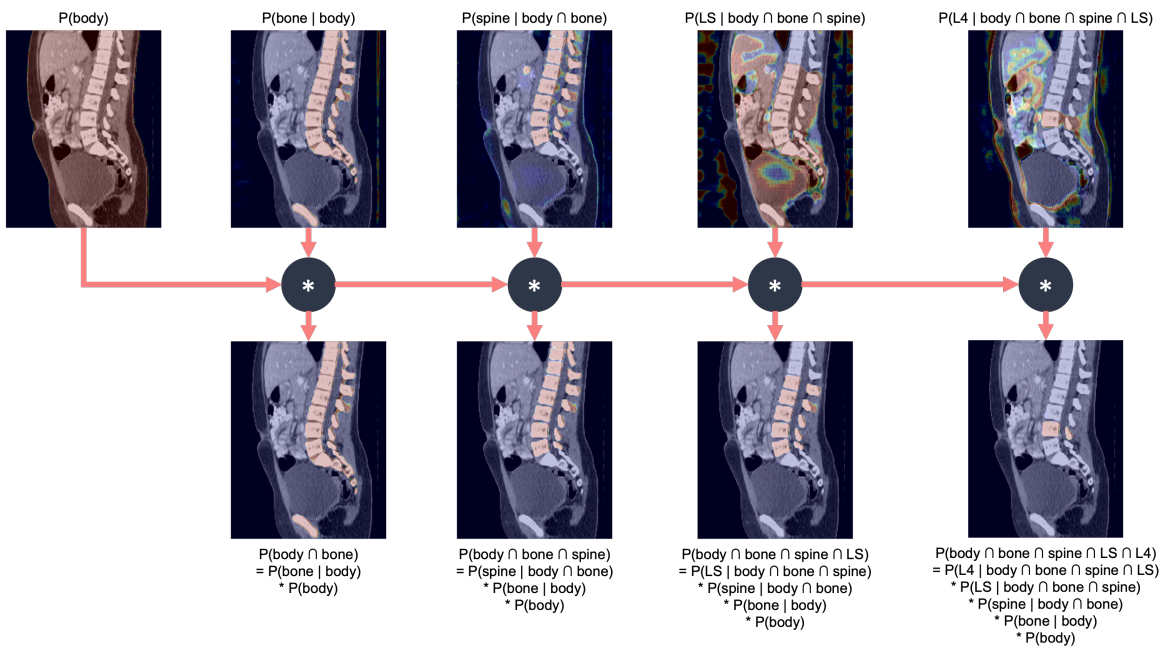


Figure 6: **Visualization of conditional probability maps for segmenting the L4 vertebra using the trained model.** In the visualization, it is showcased that the model does not directly predict the target class, but uses conditional probabilities to create the predictions. LS: Lumbar Spine.



### 3.2 Failure Analysis

In many cases, the results for the same classes varied across the datasets. To investigate these discrepancies, statistical tests were performed on datasets sharing the same labels to discover whether there were significant differences in the results. The results are reported in Table 10 of Appendix B.

An example of this discrepancy is the brain class, which however did not present a significant difference in Table 10 due to the few CT scans with this label. For the SAROS dataset, the brain class achieved a Dice score of 0.758, while for the CT-ORG dataset, it only obtained a Dice score of 0.486. This is because two CT scans of the CT-ORG dataset were classified as containing a brain segmentation by the model, but only one was annotated as such in CT-ORG. The existing segmentation achieved a Dice score of 0.973. The other case should also have been segmented, as the image, despite not showing the entire brain, still includes a visible brainstem (Figure 7B). The TotalSegmentator also produced a similar segmentation as our model (Figure 7C). In SAROS, in nine cases where the brain was not part of the CT scan, the model incorrectly predicted the brain class in other areas of the body.

In the LUNA16 dataset, the lung segmentations consistently achieved good results. However, for the middle lobe, there were some significant differences in the segmentations. In fact, sometimes the middle lobe was wrongly segmented, and in Figure 7E and Figure 7F it is possible to see that for these examples, the TotalSegmentator produced similar segmentations as our model. This is also further proven by the 0.848 Dice score of the TotalSegmentator for this class (Table 6 of Appendix B).

For the pericardium class, the annotations from the LCTSC datasets followed another definition and resulted in an overall Dice score of 0.894 compared to a Dice score of 0.952 for the SAROS dataset. According to the LCTSC guidelines, the heart is contoured around the pericardial sack. This annotation is thus not compatible with the ones produced by our model, which segments the entire area within the pericardial sack (Figure 7H).

For the bone class, where the model achieved a Dice score of 0.911 for the SAROS dataset, the Dice score for the CT-ORG dataset was 0.872. Visually, it can be seen that the model tends to include more contours than the ones from this dataset (Figure 7I, Figure 7J, and Figure 7K). In particular, our segmentations also include the cortical bone, while the TotalSegmentator and the CT-ORG segmentations tend to leave it out. Moreover, in the SAROS dataset, cartilage was annotated as bone in the rib cage, and since the rib cage is considered part of the bones, this causes a discrepancy in the segmentations. In Version 1 of the TotalSegmentator, the segmentation of the cartilage was not present, but it was added in Version 2 of the tool, as can be seen in Figure 7K.

The adrenal glands class consistently achieved the lowest Dice scores between 0.65 and 0.706. Visually, our model tends to segment a larger area that also contains the organ’s wall (Figure 7L, Figure 7M, and Figure 7N). This is also proven by the better NSD scores (between 0.887 and 0.957). For the TotalSegmentator, this class also produced similar results in the WORD dataset but had a better Dice score for the FLARE22 dataset (Table 4 of Appendix B).

For the colon segmentation, the model occasionally encountered challenges in differentiating between the colon and the small bowel. This issue is exemplified in Figure 7O and Figure 7P, where the patient underwent a right hemicolectomy, resulting in the removal of the ascending colon and a portion of the transverse colon. Due to the presence of significant air within the small bowel, the model erroneously identified it as part of the colon. However, as can be seen in Figure 7Q, the TotalSegmentator also made this mistake, even resulting in a lower Dice score for this class compared to SALT (0.773 vs. 0.808).

## 4 Discussion

In this work, we propose the SALT framework to provide a single activation layer for hierarchical probability modeling. While we have illustrated its application in medical imaging with a nnUNet model, the activation layer could be adapted to various hierarchical contexts and could be used with any model. The power of this framework lies in its ability to train a single segmentation model to recognize over 100 labels hierarchically. Throughout the training process, the loss function is computed over the full tree, allowing for the optimization of each node at every stage of training. This hierarchical training ensures that the model respects the natural structure of the data, for instance, ensuring that the colon is identified within the abdominal cavity. Additionally, the proposed model takes an average of 35 ms per slice, meaning that a full whole-body CT scan with 1000 slices can be computed in 35 seconds, which is faster than existing models [53].

### 4.1 Performance Comparison

In general, SALT obtained consistently good results for the kidneys (Dice 0.92, except for the CT-ORG dataset), the liver (Dice above 0.95), the spleen (Dice above 0.92), the stomach (Dice above 0.9), and the lungs (Dice above 0.91,

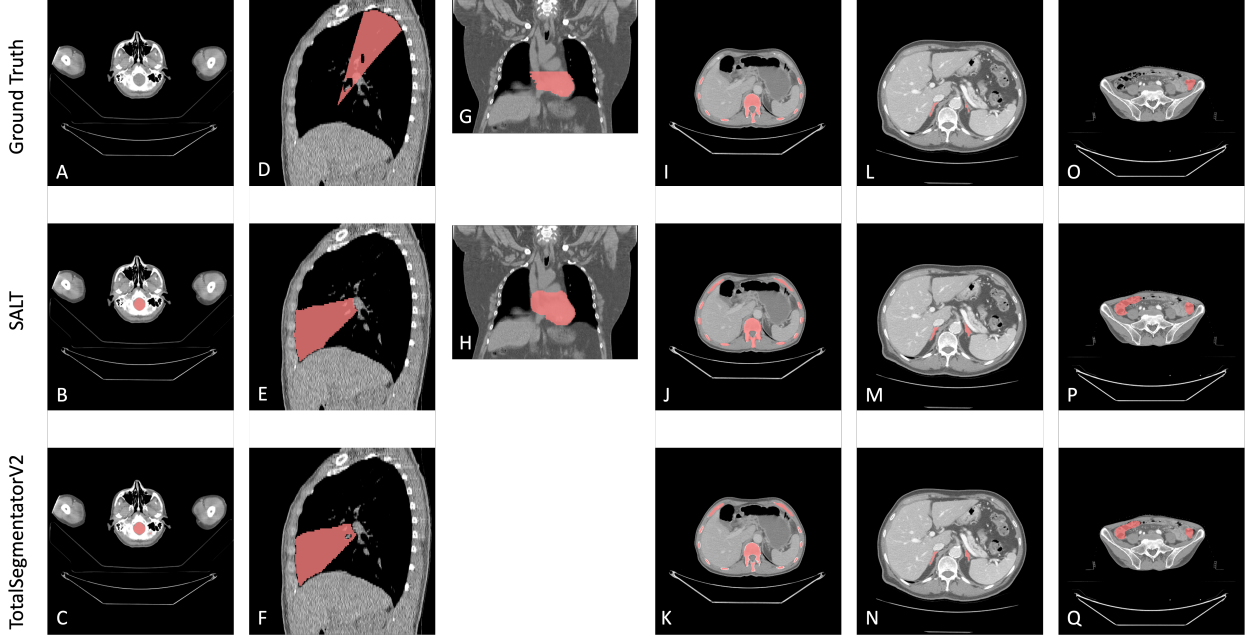


Figure 7: **Comparison between the ground truth (first row), SALT (second row) and Version 2 of the TotalSegmentator (third row).** The comparisons across various classes and datasets are systematically organized as follows: Figures A, B, and C focus on the comparison of the brain class from the CT-ORG dataset. Figures D, E, and F examine the middle lobe of the LUNA16 dataset. In Figures G and H, the analysis shifts to the pericardium from the LCTSC dataset. The bone class from the CT-ORG dataset is compared in Figures I, J, and K. Figures L, M, and N represent the adrenal glands from the FLARE22 datasets. Finally, Figures O, P, and Q compare the colon class from the WORD dataset.

except for the right middle lobe). The most difficult class to predict in terms of Dice was the adrenal glands (Dice scores of 0.65-0.70), which however showed good results for the NSD (0.88-0.95). The segmentation produced by the model tried to take more contours into account than the external dataset, yielding lower Dice scores for classes that do not account for many voxels (such as the adrenal glands).

On the SAROS dataset, SALT achieved similar results to a nnUNet-based network for BCA trained on similar classes [14]. Specifically, SALT achieved a better Dice score for the mediastinum class (0.95 vs. 0.84) and maintained a performance difference of no more than 0.05 decimal points compared to the BCA nnUNet network across most classes. The only exception was the brain class, where nnUNet achieved a higher score of 0.97 compared to SALT’s 0.75. Upon comparing SALT’s results with those of TotalSegmentator [53] for the other datasets, it was observed most classes had a difference of at most 0.05. The only exceptions were the adrenal glands and the vena cava inferior in the FLARE22 dataset, the kidneys and the urinary bladder in the CT-ORG dataset, and the brain in the SAROS dataset. Additionally, larger errors were reported in classes belonging to the gastrointestinal tract, a region traditionally challenging to segment accurately [12, 49, 51]. In fact, annotating structures such as the small and large intestines and the duodenum, presents a challenge due to their inherent complexity. These anatomical regions are notorious for their considerable variability, lack of consistent positioning, and occasional absence of clearly delineated boundaries [12, 51].

Moreover, the scores presented significant differences across the datasets, exemplifying the heterogeneity of annotation guidelines and the inherent variability of human anatomy. This is illustrated in Figure 7 and showcased by the statistical comparisons of Table 10 of Appendix B and by the results of the TotalSegmentator, with a Dice score of 0.835 for adrenal glands in the FLARE22 dataset and a score of 0.624 in the WORD dataset.

## 4.2 Clinical Applicability

The extraction of biomarkers from medical segmentations is an active field of research that has a variety of clinical applications, such as making accurate diagnoses [3], monitoring a patient’s well-being [1, 19], or predicting overall survival [17, 22]. This also includes BCA biomarkers, which are also relevant for disease progression [19, 23, 33] and predicting patient survival outcomes [15, 21]. Moreover, segmentations can also be used to predict contrast phases [4].

Given the many applications and the high volume of CT scans generated daily, models for segmentation and biomarker extraction need to prioritize speed and efficiency. SALT’s fast processing suggests that, compared to other models, it could enable quicker biomarker extraction, resulting in increased throughput. This speed could facilitate its integration into clinical workflows, enabling the automatic calculation of essential biomarkers each time a patient undergoes a CT scan.

### 4.3 Limitations & Future Work

A limitation of this study is the tendency of the model to include the walls of organs and vessels in the annotations, which differs from the annotations of the other datasets. While this approach may be advantageous for certain classes, such as bones, where it includes the cortical bone area, it may be disadvantageous for others, such as adrenal glands, where it may inadvertently include abdominal fat. This may be due to differences in annotation between the large-scale segmentations of the SALT dataset (which typically include the walls) and the TotalSegmentator predictions. Moreover, SALT also performed worse in the aorta and inferior vena cava classes (0.89 and 0.859 respectively) compared to TotalSegmentator (0.936 and 0.912 respectively). This discrepancy might be attributed to the necessity of dividing these structures into multiple regions to ensure the tree structure, which may have confused the model. This limitation arises from the required tree-like class hierarchy of the model, as not all classes are strictly assignable to a single parent node. A graph-like topology, represented by a directed acyclic graph, would greatly extend the representation capabilities, as a node could potentially have multiple parent nodes, which could be implemented as a union of all parent probabilities. However, the overall softmax properties would no longer hold, as the probabilities would not sum up to one. Another interesting extension would be to define the hierarchical tree using existing ontologies, such as the Foundational Model of Anatomy [45] or SNOMED [47], to provide standardization.

An additional extension could be used for multi-label segmentation, where each voxel gets more than one class assigned. This is especially important for overlapping concepts, such as that subcutaneous tissue or muscle can be present in all parts of the body (arms, head, legs, and torso). Moreover, this work was also intended to work with multiple datasets, such that, without any modifications, a model could be trained using different sources without needing to fuse different datasets on one single segmentation.

Furthermore, future work should aim to refine the segmentation capabilities of the model to ensure that organ walls are only included in the annotations when relevant, which raises the larger problem of unifying datasets annotated with different annotation guidelines. The introduction of advanced post-processing methods could also improve the quality of the resulting segmentations, leading to more accurate and clinically useful outcomes.

## 5 Conclusion

In conclusion, the presented SALT framework offers a new approach to medical imaging by utilizing the hierarchical nature of the human anatomy to achieve comprehensive and efficient segmentations across 113 body regions. The model’s capability to process a whole-body CT scan in an average of 35 seconds paves the way for integration into clinical workflows, enabling the immediate computation of crucial biomarkers upon performing a CT scan. While this work primarily targeted the segmentation of body regions in CT scans, SALT defines an activation function that can be used for any application or domain with a hierarchical structure. Future enhancements will focus on refining the segmentation accuracy, exploring graph-like topologies for more complex anatomical structures, and extending the model’s application to multi-label segmentation and multi-dataset integration.

## References

- [1] Juan Pablo Alderuccio, Russ A. Kuker, Fei Yang, and Craig H. Moskowitz. “Quantitative PET-based biomarkers in lymphoma: getting ready for primetime”. In: *Nature Reviews. Clinical Oncology* 20.9 (Sept. 2023), pp. 640–657. ISSN: 1759-4782. DOI: 10.1038/s41571-023-00799-2 (cit. on pp. 2, 10).
- [2] Samuel G. Armato III, Geoffrey McLennan, Luc Bidaut, Michael F. McNitt-Gray, Charles R. Meyer, et al. “The Lung Image Database Consortium (LIDC) and Image Database Resource Initiative (IDRI): A Completed Reference Database of Lung Nodules on CT Scans”. In: *Medical Physics* 38.2 (Jan. 24, 2011), pp. 915–931. ISSN: 00942405. DOI: 10.1118/1.3528204. URL: <http://doi.wiley.com/10.1118/1.3528204> (visited on 07/19/2023) (cit. on pp. 2, 3).
- [3] Afolasayo A. Aromiwura, Tyler Settle, Muhammad Umer, Jonathan Joshi, Matthew Shotwell, et al. “Artificial intelligence in cardiac computed tomography”. In: *Progress in Cardiovascular Diseases* 81 (Nov. 1, 2023), pp. 54–77. ISSN: 0033-0620. DOI: 10.1016/j.pcad.2023.09.001. URL: <https://www.sciencedirect.com/science/article/pii/S0033062023000920> (visited on 01/03/2024) (cit. on pp. 2, 10).

- [4] Giulia Baldini, René Hosch, Cynthia S Schmidt, Katarzyna Borys, Lennard Kroll, et al. “Addressing the Contrast Media Recognition Challenge: A Fully Automated Machine Learning Approach for Predicting Contrast Phases in CT Imaging”. In: *Investigative Radiology* 59.9 (2023) (cit. on p. 10).
- [5] Patrick Bilic, Patrick Christ, Hongwei Bran Li, Eugene Vorontsov, Avi Ben-Cohen, et al. “The Liver Tumor Segmentation Benchmark (LiTS)”. In: *Medical Image Analysis* 84 (Feb. 2023), p. 102680. ISSN: 13618415. DOI: 10.1016/j.media.2022.102680. arXiv: 1901.04056[cs]. URL: <http://arxiv.org/abs/1901.04056> (visited on 01/03/2024) (cit. on pp. 2, 3).
- [6] Jannis Bodden, Michael Dieckmeyer, Nico Sollmann, Egon Burian, Sebastian Rühling, et al. “Incidental vertebral fracture prediction using neuronal network-based automatic spine segmentation and volumetric bone mineral density extraction from routine clinical CT scans”. In: *Frontiers in Endocrinology* 14 (2023), p. 1207949. ISSN: 1664-2392. DOI: 10.3389/fendo.2023.1207949 (cit. on p. 2).
- [7] John S. Bridle. “Probabilistic Interpretation of Feedforward Classification Network Outputs, with Relationships to Statistical Pattern Recognition”. In: *Neurocomputing*. Ed. by Françoise Fogelman Soulié and Jeanny Héroult. NATO ASI Series. Berlin, Heidelberg: Springer, 1990, pp. 227–236. ISBN: 978-3-642-76153-9. DOI: 10.1007/978-3-642-76153-9\_28 (cit. on p. 5).
- [8] F. Busato and N. Bombieri. “Graph algorithms on GPUs”. In: *Advances in GPU Research and Practice*. Elsevier, 2017, pp. 163–198. ISBN: 978-0-12-803738-6. DOI: 10.1016/B978-0-12-803738-6.00007-0. URL: <https://linkinghub.elsevier.com/retrieve/pii/B9780128037386000070> (visited on 06/09/2023) (cit. on p. 5).
- [9] Kenneth Clark, Bruce Vendt, Kirk Smith, John Freymann, Justin Kirby, et al. “The Cancer Imaging Archive (TCIA): Maintaining and Operating a Public Information Repository”. In: *Journal of Digital Imaging* 26.6 (Dec. 2013), pp. 1045–1057. ISSN: 0897-1889, 1618-727X. DOI: 10.1007/s10278-013-9622-7. URL: <http://link.springer.com/10.1007/s10278-013-9622-7> (visited on 07/07/2023) (cit. on pp. 2, 3).
- [10] MONAI Consortium. *MONAI: Medical Open Network for AI*. Dec. 19, 2022. DOI: 10.5281/zenodo.7459814. URL: <https://zenodo.org/record/7459814> (visited on 06/02/2023) (cit. on p. 6).
- [11] Lee R. Dice. “Measures of the Amount of Ecologic Association Between Species”. In: *Ecology* 26.3 (1945). \_eprint: <https://onlinelibrary.wiley.com/doi/pdf/10.2307/1932409>, pp. 297–302. ISSN: 1939-9170. DOI: 10.2307/1932409. URL: <https://onlinelibrary.wiley.com/doi/abs/10.2307/1932409> (visited on 05/09/2023) (cit. on p. 6).
- [12] Yabo Fu, Thomas R. Mazur, Xue Wu, Shi Liu, Xiao Chang, et al. “A novel MRI segmentation method using CNN-based correction network for MRI-guided adaptive radiotherapy”. In: *Medical Physics* 45.11 (2018). \_eprint: <https://onlinelibrary.wiley.com/doi/pdf/10.1002/mp.13221>, pp. 5129–5137. ISSN: 2473-4209. DOI: 10.1002/mp.13221. URL: <https://onlinelibrary.wiley.com/doi/abs/10.1002/mp.13221> (visited on 01/31/2024) (cit. on p. 10).
- [13] Joana Guimarães, José de Almeida, Paulo Lázaro Mendes, Maria João Ferreira, and Lino Gonçalves. “Advancements in non-invasive imaging of atherosclerosis: Future perspectives”. In: *Journal of Clinical Lipidology* 0.0 (Nov. 18, 2023). Publisher: Elsevier. ISSN: 1933-2874, 1876-4789. DOI: 10.1016/j.jacl.2023.11.008. URL: <https://doi.org/10.1016/j.jacl.2023.11.008> (cit. on p. 2).
- [14] Johannes Haubold, Giulia Baldini, Vicky Parmar, Benedikt Michael Schaarschmidt, Sven Koitka, et al. “BOA: A CT-Based Body and Organ Analysis for Radiologists at the Point of Care”. In: *Investigative Radiology* 59.6 (2024). DOI: 10.1097/RLI.0000000000001040. URL: <http://doi.org/10.1097/RLI.0000000000001040> (cit. on pp. 2, 10).
- [15] René Hosch, Simone Kattner, Marc Moritz Berger, Thorsten Brenner, Johannes Haubold, et al. “Biomarkers extracted by fully automated body composition analysis from chest CT correlate with SARS-CoV-2 outcome severity”. In: *Scientific Reports* 12.1 (Sept. 30, 2022), p. 16411. ISSN: 2045-2322. DOI: 10.1038/s41598-022-20419-w (cit. on pp. 2, 10).
- [16] Fabian Isensee, Paul F. Jaeger, Simon A. A. Kohl, Jens Petersen, and Klaus H. Maier-Hein. “nnU-Net: a self-configuring method for deep learning-based biomedical image segmentation”. In: *Nature Methods* 18.2 (2021), pp. 203–211. ISSN: 1548-7105. DOI: 10.1038/s41592-020-01008-z. URL: <https://www.nature.com/articles/s41592-020-01008-z> (visited on 07/07/2023) (cit. on pp. 2, 6).
- [17] Takahiro Ito, Akihiro Tanemura, Toru Kuramitsu, Taichi Murase, Benson Kaluba, et al. “Spleen volume is a predictor of posthepatectomy liver failure and short-term mortality for hepatocellular carcinoma”. In: *Langenbeck’s Archives of Surgery* 408.1 (Aug. 7, 2023), p. 297. ISSN: 1435-2451. DOI: 10.1007/s00423-023-03025-w (cit. on pp. 2, 10).
- [18] Yan-Wei Jiang, Xiong-Jie Xu, Rui Wang, and Chun-Mei Chen. “Radiomics analysis based on lumbar spine CT to detect osteoporosis”. In: *European Radiology* 32.11 (Nov. 2022), pp. 8019–8026. ISSN: 1432-1084. DOI: 10.1007/s00330-022-08805-4 (cit. on p. 2).

- [19] Han Na Jung, Yun Kyung Cho, Hwi Seung Kim, Eun Hee Kim, Min Jung Lee, et al. “Association between hypertension and myosteatosi s evaluated by abdominal computed tomography”. In: *Hypertension Research* 46.4 (Apr. 2023). Number: 4 Publisher: Nature Publishing Group, pp. 845–855. ISSN: 1348-4214. DOI: 10.1038/s41440-022-01157-y. URL: <https://www.nature.com/articles/s41440-022-01157-y> (visited on 01/03/2024) (cit. on pp. 2, 10).
- [20] Jacqueline C. Junn, Karl A. Soderlund, and Christine M. Glastonbury. “Imaging of Head and Neck Cancer With CT, MRI, and US”. In: *Seminars in Nuclear Medicine*. Imaging Options for Head and Neck Cancer 51.1 (Jan. 1, 2021), pp. 3–12. ISSN: 0001-2998. DOI: 10.1053/j.semnuclmed.2020.07.005. URL: <https://www.sciencedirect.com/science/article/pii/S0001299820300763> (visited on 12/28/2023) (cit. on p. 2).
- [21] Julius Keyl, René Hosch, Aaron Berger, Oliver Ester, Tobias Greiner, et al. “Deep learning-based assessment of body composition and liver tumour burden for survival modelling in advanced colorectal cancer”. In: *Journal of Cachexia, Sarcopenia and Muscle* 14.1 (Feb. 2023), pp. 545–552. ISSN: 2190-6009. DOI: 10.1002/jcsm.13158 (cit. on pp. 2, 10).
- [22] P. Khoshpouri, B. Hazhirkarzar, S. Ameli, A. Pandey, M. Ghadimi, et al. “Quantitative spleen and liver volume changes predict survival of patients with primary sclerosing cholangitis”. In: *Clinical Radiology* 74.9 (Sept. 2019), 734.e13–734.e20. ISSN: 1365-229X. DOI: 10.1016/j.crad.2019.05.018 (cit. on pp. 2, 10).
- [23] Yousun Ko, Heeryoel Jeong, Seungwoo Khang, Jeongjin Lee, Kyung Won Kim, et al. “Change of Computed Tomography-Based Body Composition after Adrenalectomy in Patients with Pheochromocytoma”. In: *Cancers* 14.8 (Apr. 13, 2022), p. 1967. ISSN: 2072-6694. DOI: 10.3390/cancers14081967 (cit. on pp. 2, 10).
- [24] Sven Koitka, Giulia Baldini, Lennard Kroll, Natalie van Landeghem, Johannes Haubold, et al. *SAROS - A large, heterogeneous, and sparsely annotated segmentation dataset on CT imaging data (SAROS)*. Version 1. 2023. DOI: 10.25737/SZ96-ZG60. URL: <https://wiki.cancerimagingarchive.net/x/2wVgCQ> (visited on 09/26/2023) (cit. on p. 3).
- [25] Sven Koitka, Giulia Baldini, Lennard Kroll, Natalie van Landeghem, Olivia B. Pollok, et al. “SAROS: A dataset for whole-body region and organ segmentation in CT imaging”. In: *Scientific Data* 11.1 (May 10, 2024). Publisher: Nature Publishing Group, p. 483. ISSN: 2052-4463. DOI: 10.1038/s41597-024-03337-6. URL: <https://www.nature.com/articles/s41597-024-03337-6> (visited on 07/05/2024) (cit. on pp. 2, 3).
- [26] Sven Koitka, Phillip Gudlin, Jens M. Theysohn, Arzu Oezcelik, Dieter P. Hoyer, et al. “Fully automated preoperative liver volumetry incorporating the anatomical location of the central hepatic vein”. In: *Scientific Reports* 12.1 (Oct. 1, 2022), p. 16479. ISSN: 2045-2322. DOI: 10.1038/s41598-022-20778-4 (cit. on p. 2).
- [27] Sven Koitka, Lennard Kroll, Eugen Malamutmann, Arzu Oezcelik, and Felix Nensa. “Fully automated body composition analysis in routine CT imaging using 3D semantic segmentation convolutional neural networks”. In: *European Radiology* 31.4 (Apr. 2021), pp. 1795–1804. ISSN: 1432-1084. DOI: 10.1007/s00330-020-07147-3 (cit. on p. 2).
- [28] Ilya Loshchilov and Frank Hutter. *Decoupled Weight Decay Regularization*. Jan. 4, 2019. DOI: 10.48550/arXiv.1711.05101. arXiv: 1711.05101[cs,math]. URL: <http://arxiv.org/abs/1711.05101> (visited on 06/13/2023) (cit. on p. 6).
- [29] Ilya Loshchilov and Frank Hutter. *SGDR: Stochastic Gradient Descent with Warm Restarts*. May 3, 2017. DOI: 10.48550/arXiv.1608.03983. arXiv: 1608.03983[cs,math]. URL: <http://arxiv.org/abs/1608.03983> (visited on 06/12/2023) (cit. on p. 6).
- [30] Xiangde Luo, Wenjun Liao, Jianghong Xiao, Jieneng Chen, Tao Song, et al. “WORD: A large scale dataset, benchmark and clinical applicable study for abdominal organ segmentation from CT image”. In: *Medical Image Analysis* 82 (Nov. 1, 2022), p. 102642. ISSN: 1361-8415. DOI: 10.1016/j.media.2022.102642. URL: <https://www.sciencedirect.com/science/article/pii/S1361841522002705> (visited on 01/03/2024) (cit. on pp. 2, 3).
- [31] Jun Ma. *MICCAI FLARE22 Challenge Dataset (50 Labeled Abdomen CT Scans)*. Version 1.0. Apr. 24, 2023. DOI: 10.5281/zenodo.7860267. URL: <https://zenodo.org/records/7860267> (visited on 01/03/2024) (cit. on pp. 2, 3).
- [32] Jun Ma, Yao Zhang, Song Gu, Cheng Ge, Shihao Ma, et al. *Unleashing the Strengths of Unlabeled Data in Pan-cancer Abdominal Organ Quantification: the FLARE22 Challenge*. Aug. 10, 2023. DOI: 10.48550/arXiv.2308.05862. arXiv: 2308.05862[cs, eess]. URL: <http://arxiv.org/abs/2308.05862> (visited on 01/03/2024) (cit. on pp. 2, 3).
- [33] Stefanie Elizabeth Mason, Rafael Moreta-Martinez, Wassim W. Labaki, Matthew Strand, David Baraghoshi, et al. “Respiratory exacerbations are associated with muscle loss in current and former smokers”. In: *Thorax* 76.6 (June 2021), pp. 554–560. ISSN: 1468-3296. DOI: 10.1136/thoraxjnl-2020-215999 (cit. on pp. 2, 10).

- [34] Fausto Milletari, Nassir Navab, and Seyed-Ahmad Ahmadi. “V-Net: Fully Convolutional Neural Networks for Volumetric Medical Image Segmentation”. In: *2016 Fourth International Conference on 3D Vision (3DV)*. 2016 Fourth International Conference on 3D Vision (3DV). Oct. 2016, pp. 565–571. DOI: 10.1109/3DV.2016.79 (cit. on p. 6).
- [35] Kevin P. Murphy. “Information Theory”. In: *Probabilistic Machine Learning: An introduction*. MIT Press, 2022, pp. 203–205. ISBN: 978-0-262-04682-4. URL: [probml.ai](http://probml.ai) (cit. on p. 6).
- [36] Jakob Neubauer, Caroline Wilpert, Oliver Gebler, Florin-Andrei Taran, Martin Pichotka, et al. “Diagnostic Accuracy of Contrast-Enhanced Thoracic Photon-Counting Computed Tomography for Opportunistic Locoregional Staging of Breast Cancer Compared With Digital Mammography: A Prospective Trial”. In: *Investigative Radiology* (Dec. 1, 2023). ISSN: 1536-0210. DOI: 10.1097/RLI.0000000000001051. URL: <https://doi.org/10.1097/RLI.0000000000001051> (cit. on p. 2).
- [37] Stanislav Nikolov, Sam Blackwell, Alexei Zverovitch, Ruheena Mendes, Michelle Livne, et al. “Clinically Applicable Segmentation of Head and Neck Anatomy for Radiotherapy: Deep Learning Algorithm Development and Validation Study”. In: *Journal of Medical Internet Research* 23.7 (July 12, 2021), e26151. ISSN: 1438-8871. DOI: 10.2196/26151 (cit. on p. 6).
- [38] Sebastian Nowak, Anton Faron, Julian A. Luetkens, Helena L. Geißler, Michael Praktiknjo, et al. “Fully Automated Segmentation of Connective Tissue Compartments for CT-Based Body Composition Analysis: A Deep Learning Approach”. In: *Investigative Radiology* 55.6 (June 2020), pp. 357–366. ISSN: 1536-0210. DOI: 10.1097/RLI.0000000000000647 (cit. on p. 2).
- [39] Sebastian Nowak, Maike Theis, Barbara D. Wichtmann, Anton Faron, Matthias F. Froelich, et al. “End-to-end automated body composition analyses with integrated quality control for opportunistic assessment of sarcopenia in CT”. In: *European Radiology* 32.5 (2022), pp. 3142–3151. ISSN: 0938-7994. DOI: 10.1007/s00330-021-08313-x. URL: <https://www.ncbi.nlm.nih.gov/pmc/articles/PMC9038788/> (visited on 08/25/2023) (cit. on p. 2).
- [40] NVIDIA Corporation. *NVIDIA RTX A6000 Powered by Ampere Architecture*. NVIDIA. 2024. URL: <https://www.nvidia.com/en-us/design-visualization/rtx-a6000/> (visited on 01/26/2024) (cit. on p. 7).
- [41] Maia Osborne-Grinter, Adnan Ali, and Michelle C. Williams. “Prevalence and clinical implications of coronary artery calcium scoring on non-gated thoracic computed tomography: a systematic review and meta-analysis”. In: *European Radiology* (Dec. 22, 2023). ISSN: 1432-1084. DOI: 10.1007/s00330-023-10439-z. URL: <https://doi.org/10.1007/s00330-023-10439-z> (cit. on p. 2).
- [42] Adam Paszke, Sam Gross, Francisco Massa, Adam Lerer, James Bradbury, et al. “PyTorch: An Imperative Style, High-Performance Deep Learning Library”. In: *Advances in Neural Information Processing Systems*. Vol. 32. Curran Associates, Inc., 2019. URL: [https://proceedings.neurips.cc/paper\\_files/paper/2019/hash/bdbca288fee7f92f2bfa9f7012727740-Abstract.html](https://proceedings.neurips.cc/paper_files/paper/2019/hash/bdbca288fee7f92f2bfa9f7012727740-Abstract.html) (visited on 06/02/2023) (cit. on p. 6).
- [43] Keyur Radiya, Henrik Lykke Joakimsen, Karl Øyvind Mikalsen, Eirik Kjus Aahlin, Rolv-Ole Lindsetmo, et al. “Performance and clinical applicability of machine learning in liver computed tomography imaging: a systematic review”. In: *European Radiology* 33.10 (Oct. 2023), pp. 6689–6717. ISSN: 1432-1084. DOI: 10.1007/s00330-023-09609-w (cit. on p. 2).
- [44] Blaine Rister, Darvin Yi, Kaushik Shivakumar, Tomomi Nobashi, and Daniel L. Rubin. “CT-ORG, a new dataset for multiple organ segmentation in computed tomography”. In: *Scientific Data* 7.1 (Nov. 11, 2020). Number: 1 Publisher: Nature Publishing Group, p. 381. ISSN: 2052-4463. DOI: 10.1038/s41597-020-00715-8. URL: <https://www.nature.com/articles/s41597-020-00715-8> (visited on 08/25/2023) (cit. on pp. 2, 3).
- [45] Cornelius Rosse and José L. V. Mejino. “The Foundational Model of Anatomy Ontology”. In: *Anatomy Ontologies for Bioinformatics: Principles and Practice*. Ed. by Albert Burger, Duncan Davidson, and Richard Baldock. London: Springer, 2008, pp. 59–117. ISBN: 978-1-84628-885-2. DOI: 10.1007/978-1-84628-885-2\_4. URL: [https://doi.org/10.1007/978-1-84628-885-2\\_4](https://doi.org/10.1007/978-1-84628-885-2_4) (visited on 03/27/2024) (cit. on p. 11).
- [46] Stuart J. Russell and Peter Norvig. “Probabilistic Reasoning”. In: *Artificial intelligence: a modern approach*. 3rd ed. Prentice Hall series in artificial intelligence. Upper Saddle River: Prentice Hall, 2010, pp. 510–515. ISBN: 978-0-13-604259-4 (cit. on p. 5).
- [47] Shaker El-Sappagh, Francesco Franda, Farman Ali, and Kyung-Sup Kwak. “SNOMED CT standard ontology based on the ontology for general medical science”. In: *BMC Medical Informatics and Decision Making* 18.1 (Aug. 31, 2018), p. 76. ISSN: 1472-6947. DOI: 10.1186/s12911-018-0651-5. URL: <https://doi.org/10.1186/s12911-018-0651-5> (visited on 12/13/2023) (cit. on p. 11).
- [48] Laura Schöckel, Gregor Jost, Peter Seidensticker, Philipp Lengsfeld, Petra Palkowitsch, et al. “Developments in X-Ray Contrast Media and the Potential Impact on Computed Tomography”. In: *Investigative Radiology* 55.9 (Sept. 2020), pp. 592–597. ISSN: 1536-0210. DOI: 10.1097/RLI.0000000000000696 (cit. on p. 2).

- [49] Efaza Siddiqui. “Differentiating Large from Small Bowel”. In: *Essential Radiology Review: A Question and Answer Guide*. Ed. by Adam E. M. Eltorai, Charles H. Hyman, and Terrance T. Healey. Cham: Springer International Publishing, 2019, pp. 273–274. ISBN: 978-3-030-26044-6. DOI: 10.1007/978-3-030-26044-6\_78. URL: [https://doi.org/10.1007/978-3-030-26044-6\\_78](https://doi.org/10.1007/978-3-030-26044-6_78) (visited on 01/31/2024) (cit. on p. 10).
- [50] Hao Tang, Chupeng Zhang, and Xiaohui Xie. *Automatic Pulmonary Lobe Segmentation Using Deep Learning*. Apr. 10, 2019. DOI: 10.48550/arXiv.1903.09879. arXiv: 1903.09879[cs]. URL: <http://arxiv.org/abs/1903.09879> (visited on 01/03/2024) (cit. on pp. 2, 3).
- [51] Chong Wang, Zhiming Cui, Junwei Yang, Miaofei Han, Gustavo Carneiro, et al. “BowelNet: Joint Semantic-Geometric Ensemble Learning for Bowel Segmentation From Both Partially and Fully Labeled CT Images”. In: *IEEE transactions on medical imaging* 42.4 (Apr. 2023), pp. 1225–1236. ISSN: 1558-254X. DOI: 10.1109/TMI.2022.3225667 (cit. on p. 10).
- [52] Jakob Wasserthal. *Dataset with segmentations of 104 important anatomical structures in 1204 CT images*. Version 1.0. July 6, 2022. DOI: 10.5281/zenodo.6802614. URL: <https://zenodo.org/record/6802614> (visited on 05/09/2023) (cit. on p. 2).
- [53] Jakob Wasserthal, Hanns-Christian Breit, Manfred T. Meyer, Maurice Pradella, Daniel Hinck, et al. “TotalSegmentator: Robust Segmentation of 104 Anatomic Structures in CT Images”. In: *Radiology: Artificial Intelligence* 5.5 (Sept. 2023). Publisher: Radiological Society of North America, e230024. DOI: 10.1148/ryai.230024. URL: <https://pubs.rsna.org/doi/10.1148/ryai.230024> (visited on 11/07/2023) (cit. on pp. 2, 6, 9, 10).
- [54] Jinzhong Yang, Greg Sharp, Harini Veeraraghavan, Wouter Van Elmpt, Andre Dekker, et al. *Data from Lung CT Segmentation Challenge 2017 (LCTSC)*. In collab. with TCIA Team. Version 3. 2017. DOI: 10.7937/K9/TCIA.2017.3R3FVZ08. URL: <https://www.cancerimagingarchive.net/collection/lctsc/> (visited on 01/03/2024) (cit. on pp. 2, 3).
- [55] Jinzhong Yang, Harini Veeraraghavan, Samuel G. Armato, Keyvan Farahani, Justin S. Kirby, et al. “Autosegmentation for thoracic radiation treatment planning: A grand challenge at AAPM 2017”. In: *Medical Physics* 45.10 (Oct. 2018), pp. 4568–4581. ISSN: 0094-2405. DOI: 10.1002/mp.13141. URL: <https://www.ncbi.nlm.nih.gov/pmc/articles/PMC6714977/> (visited on 08/25/2023) (cit. on pp. 2, 3).

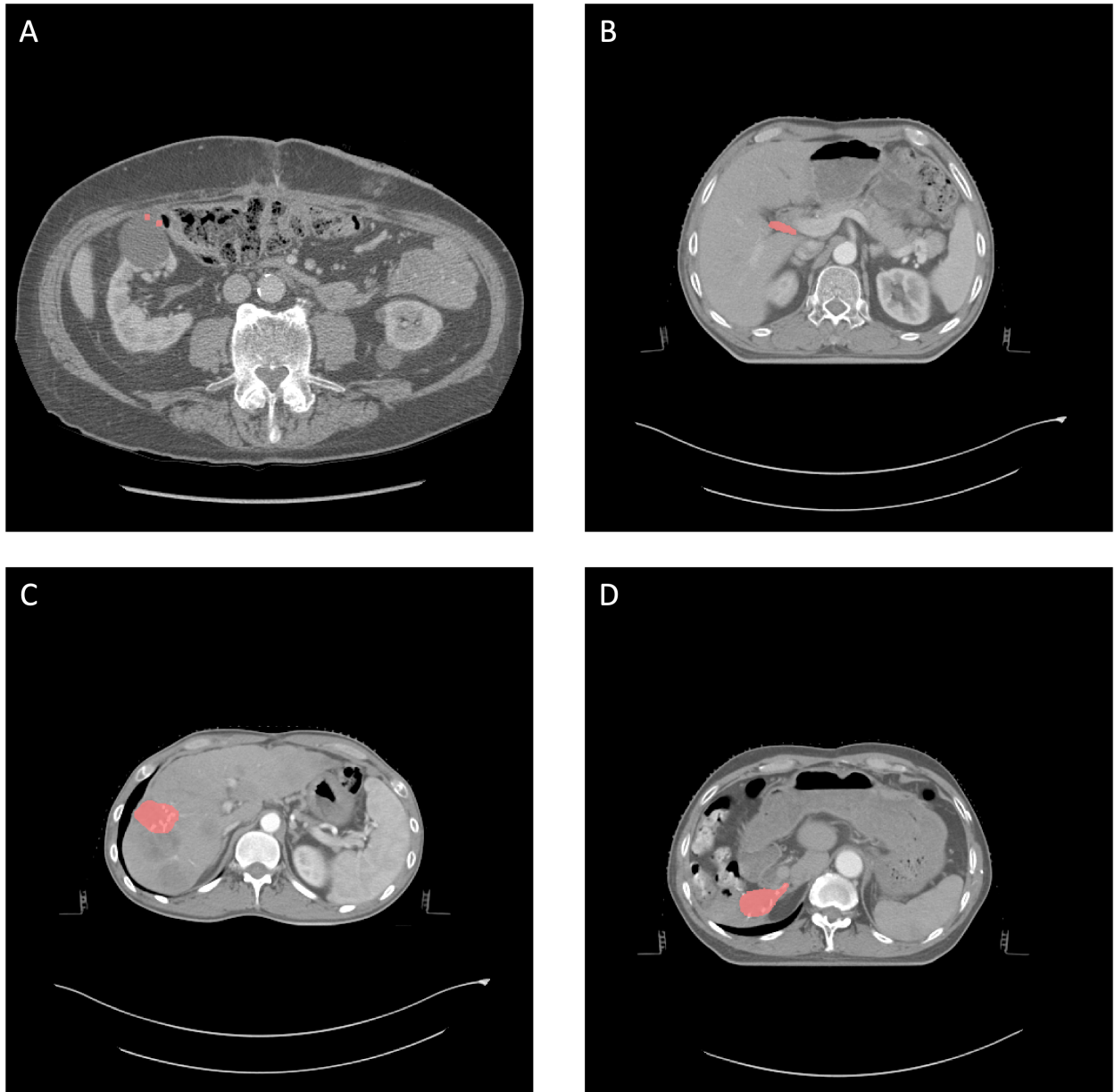
**A Additional Figures**

Figure 8: **Gallbladder Segmentations of the WORD dataset.** In A, 5 voxels were marked as gallbladder and binary dilation was performed to be able to visualize them. In B and D, the common bile duct was segmented instead of the gallbladder. In C, a tumor was identified as the gallbladder.



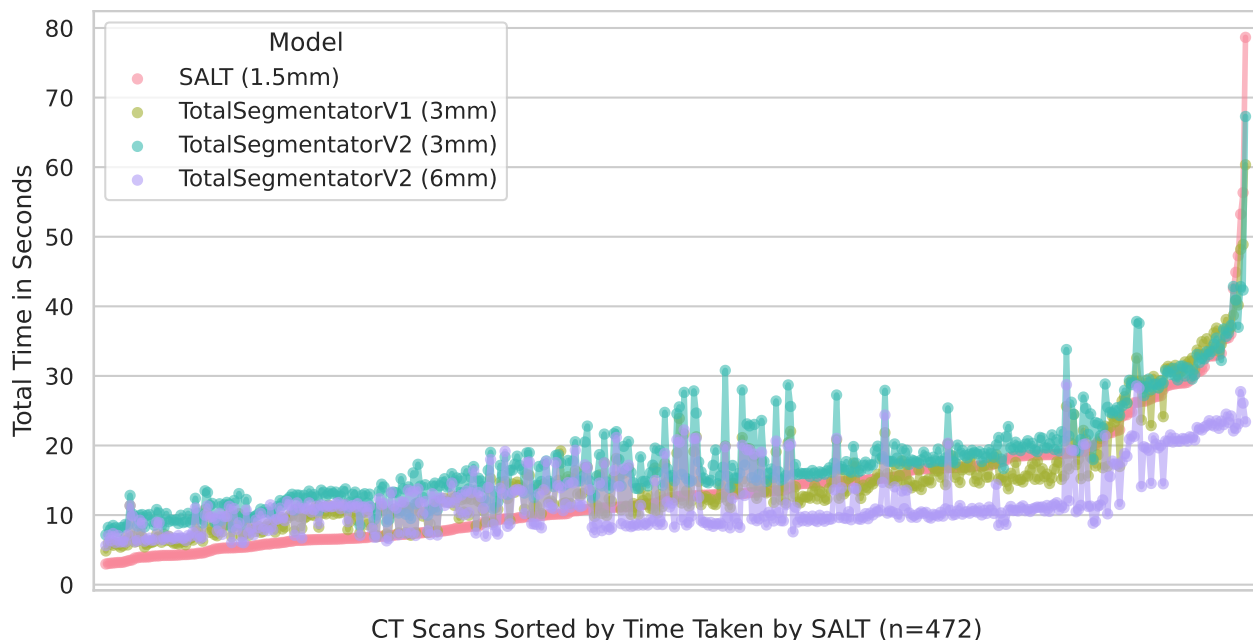


Figure 9: **Comparison between the speed of SALT and the TotalSegmentator.** The fast alternatives of the TotalSegmentator were run on the same set of 472 CT scans from Table 1. Version 1 only has a fast alternative that uses one single model and 3mm isotropic spacing, while Version 2 has two alternatives that use 3mm and 6mm isotropic spacing.

## B Additional Tables

Table 3: **Dice scores and Normalized Surface Dice (NSD) for the CT-ORG dataset.** The scores are reported for SALT and Version 2 of the TotalSegmentator (TSV2). The 95% confidence intervals are reported in brackets.

Label	SALT (Dice)	TSV2 (Dice)	SALT (NSD)	TSV2 (NSD)
Kidneys	0.872 [0.854, 0.884]	0.927 [0.912, 0.94]	0.914 [0.884, 0.937]	0.951 [0.92, 0.975]
Liver	0.95 [0.946, 0.953]	0.964 [0.961, 0.967]	0.92 [0.906, 0.935]	0.952 [0.945, 0.961]
Urinary Bladder	0.829 [0.787, 0.867]	0.881 [0.853, 0.905]	0.731 [0.655, 0.805]	0.858 [0.8, 0.906]
Bones	0.872 [0.863, 0.879]	0.877 [0.861, 0.89]	0.919 [0.912, 0.926]	0.883 [0.866, 0.897]
Brain	0.486 [0, 0.973]	0.488 [0, 0.976]	0.49 [0, 0.981]	0.492 [0, 0.985]
Lungs	0.962 [0.958, 0.966]	0.97 [0.964, 0.975]	0.968 [0.951, 0.982]	0.971 [0.955, 0.984]

Table 4: **Dice scores and Normalized Surface Dice (NSD) for the FLARE22 dataset.** The scores are reported for SALT and Version 2 of the TotalSegmentator (TSV2). The 95% confidence intervals are reported in brackets.

Label	SALT (Dice)	TSV2 (Dice)	SALT (NSD)	TSV2 (NSD)
Adrenal Glands	0.699 [0.683, 0.713]	0.835 [0.825, 0.846]	0.949 [0.935, 0.961]	0.978 [0.969, 0.986]
Adrenal Gland (L)	0.693 [0.674, 0.709]	0.837 [0.824, 0.849]	0.944 [0.925, 0.959]	0.978 [0.965, 0.988]
Adrenal Gland (R)	0.706 [0.687, 0.724]	0.831 [0.814, 0.845]	0.957 [0.944, 0.97]	0.978 [0.965, 0.988]
Duodenum	0.756 [0.74, 0.77]	0.768 [0.749, 0.785]	0.836 [0.821, 0.852]	0.844 [0.828, 0.86]
Gallbladder	0.861 [0.844, 0.877]	0.894 [0.878, 0.91]	0.956 [0.942, 0.969]	0.958 [0.941, 0.973]
Kidneys	0.92 [0.913, 0.925]	0.915 [0.899, 0.929]	0.959 [0.948, 0.968]	0.938 [0.922, 0.953]
Kidney (L)	0.919 [0.914, 0.924]	0.914 [0.897, 0.928]	0.963 [0.954, 0.97]	0.94 [0.924, 0.955]
Kidney (R)	0.921 [0.912, 0.928]	0.921 [0.899, 0.936]	0.956 [0.943, 0.967]	0.939 [0.919, 0.955]
Liver	0.952 [0.95, 0.954]	0.972 [0.971, 0.973]	0.966 [0.96, 0.97]	0.977 [0.975, 0.979]
Pancreas	0.843 [0.83, 0.856]	0.833 [0.815, 0.85]	0.934 [0.92, 0.946]	0.929 [0.91, 0.945]
Spleen	0.94 [0.935, 0.943]	0.974 [0.972, 0.975]	0.972 [0.966, 0.978]	0.999 [0.998, 0.999]
Stomach	0.93 [0.925, 0.935]	0.954 [0.949, 0.958]	0.974 [0.967, 0.979]	0.982 [0.976, 0.987]
Aorta	0.89 [0.882, 0.896]	0.936 [0.926, 0.945]	0.951 [0.937, 0.962]	0.958 [0.94, 0.973]
Vena Cava Inferior	0.859 [0.854, 0.865]	0.912 [0.905, 0.918]	0.942 [0.934, 0.949]	0.954 [0.946, 0.96]

Table 5: **Dice scores and Normalized Surface Dice (NSD) for the LCTSC dataset.** The scores are reported for SALT and Version 2 of the TotalSegmentator (TSV2). The 95% confidence intervals are reported in brackets. (L) = Left, (R) = Right.

Label	SALT (Dice)	TSV2 (Dice)	SALT (NSD)	TSV2 (NSD)
Spinal Cord	0.84 [0.833, 0.845]	0.881 [0.874, 0.886]	0.969 [0.963, 0.975]	0.977 [0.971, 0.981]
Lungs	0.941 [0.934, 0.947]	0.959 [0.953, 0.965]	0.894 [0.877, 0.909]	0.937 [0.925, 0.949]
Lung (L)	0.922 [0.9, 0.94]	0.948 [0.933, 0.96]	0.878 [0.849, 0.904]	0.929 [0.908, 0.948]
Lung (R)	0.946 [0.937, 0.952]	0.961 [0.953, 0.967]	0.896 [0.877, 0.913]	0.938 [0.921, 0.952]
Pericardium	0.894 [0.887, 0.901]	/	0.792 [0.769, 0.815]	/

Table 6: **Dice scores and Normalized Surface Dice (NSD) for the LUNA16 dataset.** The scores are reported for SALT and Version 2 of the TotalSegmentator (TSV2). The 95% confidence intervals are reported in brackets. (L) = Left, (R) = Right.

Label	SALT (Dice)	TSV2 (Dice)	SALT (NSD)	TSV2 (NSD)
Lungs	0.961 [0.956, 0.964]	0.983 [0.981, 0.984]	0.951 [0.935, 0.962]	0.979 [0.976, 0.982]
Lung (L)	0.956 [0.949, 0.961]	0.982 [0.979, 0.984]	0.945 [0.926, 0.958]	0.981 [0.977, 0.983]
Lung Lower Lobe (L)	0.931 [0.917, 0.94]	0.961 [0.956, 0.966]	0.905 [0.875, 0.927]	0.953 [0.941, 0.964]
Lung Upper Lobe (L)	0.948 [0.943, 0.952]	0.969 [0.966, 0.971]	0.943 [0.93, 0.953]	0.962 [0.952, 0.97]
Lung (R)	0.964 [0.96, 0.967]	0.984 [0.982, 0.985]	0.956 [0.943, 0.965]	0.978 [0.975, 0.981]
Lung Lower Lobe (R)	0.93 [0.918, 0.938]	0.955 [0.948, 0.962]	0.894 [0.871, 0.912]	0.926 [0.913, 0.939]
Lung Middle Lobe (R)	0.835 [0.787, 0.873]	0.848 [0.8, 0.885]	0.794 [0.75, 0.835]	0.806 [0.763, 0.842]
Lung Upper Lobe (R)	0.916 [0.894, 0.931]	0.933 [0.911, 0.947]	0.874 [0.845, 0.898]	0.888 [0.862, 0.911]

Table 7: **Dice scores and Normalized Surface Dice (NSD) for the SAROS dataset.** The scores are reported for SALT and Version 2 of the TotalSegmentator (TSV2). The 95% confidence intervals are reported in brackets.

Label	SALT (Dice)	TSV2 (Dice)	SALT (NSD)	TSV2 (NSD)
Abdominal Cavity	0.98 [0.979, 0.981]	/	0.995 [0.994, 0.995]	/
Bones	0.911 [0.908, 0.914]	0.805 [0.8, 0.811]	0.991 [0.99, 0.992]	0.942 [0.938, 0.945]
Brain	0.758 [0.656, 0.858]	0.939 [0.886, 0.974]	0.794 [0.691, 0.896]	0.964 [0.91, 0.996]
Muscles	0.931 [0.928, 0.934]	/	0.989 [0.987, 0.991]	/
Spinal Cord	0.849 [0.845, 0.852]	0.878 [0.872, 0.885]	0.975 [0.972, 0.978]	0.964 [0.958, 0.97]
Subcutaneous Tissue	0.937 [0.932, 0.942]	/	0.991 [0.989, 0.993]	/
Thoracic Cavity	0.972 [0.969, 0.975]	/	0.992 [0.99, 0.994]	/
Mediastinum	0.95 [0.944, 0.955]	/	0.981 [0.976, 0.984]	/
Pericardium	0.952 [0.949, 0.955]	/	0.982 [0.979, 0.984]	/

Table 8: **Dice scores and Normalized Surface Dice (NSD) for the WORD dataset.** The scores are reported for SALT and Version 2 of the TotalSegmentator (TSV2). The 95% confidence intervals are reported in brackets. (L) = Left, (R) = Right.

Label	SALT (Dice)	TSV2 (Dice)	SALT (NSD)	TSV2 (NSD)
Adrenal Glands	0.65 [0.631, 0.667]	0.624 [0.603, 0.643]	0.887 [0.868, 0.903]	0.856 [0.833, 0.875]
Colon	0.808 [0.796, 0.819]	0.773 [0.76, 0.785]	0.828 [0.814, 0.841]	0.784 [0.768, 0.798]
Duodenum	0.642 [0.619, 0.662]	0.623 [0.598, 0.644]	0.741 [0.719, 0.761]	0.718 [0.692, 0.74]
Kidneys	0.923 [0.917, 0.926]	0.925 [0.921, 0.928]	0.97 [0.963, 0.974]	0.973 [0.968, 0.977]
Kidney (L)	0.922 [0.914, 0.928]	0.922 [0.918, 0.926]	0.971 [0.961, 0.978]	0.969 [0.963, 0.974]
Kidney (R)	0.922 [0.92, 0.925]	0.927 [0.923, 0.931]	0.969 [0.965, 0.972]	0.976 [0.971, 0.98]
Liver	0.951 [0.949, 0.953]	0.956 [0.954, 0.957]	0.952 [0.946, 0.958]	0.96 [0.956, 0.963]
Pancreas	0.802 [0.79, 0.812]	0.791 [0.782, 0.8]	0.922 [0.914, 0.93]	0.911 [0.903, 0.918]
Small Bowel	0.821 [0.81, 0.83]	0.797 [0.784, 0.81]	0.867 [0.855, 0.878]	0.847 [0.831, 0.863]
Spleen	0.927 [0.924, 0.93]	0.939 [0.937, 0.942]	0.962 [0.956, 0.968]	0.986 [0.983, 0.989]
Stomach	0.9 [0.89, 0.907]	0.904 [0.898, 0.91]	0.925 [0.914, 0.935]	0.93 [0.922, 0.938]
Urinary Bladder	0.864 [0.843, 0.882]	0.903 [0.884, 0.918]	0.914 [0.894, 0.931]	0.96 [0.945, 0.971]

Table 9: **Evaluation of the time taken by the model at inference time.** The inference and total time are reported in seconds, and all values are given as mean  $\pm$  standard deviation. The times and the number of slices were stored after preprocessing the CT scan to a spacing of (1.5, 1.5, 1.5).

	CT-ORG	FLARE22	LCTSC	LUNA16	SAROS	WORD
Inference Time	8.87 $\pm$ 11.88	2.84 $\pm$ 1.19	8.89 $\pm$ 2.84	2.74 $\pm$ 1.03	8.86 $\pm$ 7.68	10.25 $\pm$ 2.83
Total Time	17.73 $\pm$ 14.77	4.95 $\pm$ 1.46	13.21 $\pm$ 3.56	6.96 $\pm$ 2.01	15.95 $\pm$ 11.63	15.93 $\pm$ 3.03
Number Slices	396.19 $\pm$ 187.16	167.64 $\pm$ 39.19	273.76 $\pm$ 37.0	208.68 $\pm$ 26.94	359.05 $\pm$ 183.77	385.44 $\pm$ 61.75
Seconds per Slice	0.04 $\pm$ 0.01	0.02 $\pm$ 0.008	0.04 $\pm$ 0.01	0.03 $\pm$ 0.009	0.04 $\pm$ 0.01	0.04 $\pm$ 0.003

Table 10: **Results of the statistical tests for the Dice score and the Normalized Surface Dice (NSD) across the datasets.** For organs present in multiple datasets, the results across these datasets were compared using statistical tests. The comparisons were conducted either using the Mann-Whitney U test (for labels belonging to two datasets) or with the Kruskal-Wallis test with Dunn’s post-hoc multiple comparison test adjustment (for more than two datasets). Moreover, the p-values were adjusted for multiple comparisons using Bonferroni’s method. A star (\*) denotes statistically significant differences in results between the reported datasets for a particular organ label. In all cases, p-values less than or equal to 0.05 were considered significant.

	<b>Dice</b>	<b>NSD</b>
Adrenal Glands	FLARE22 vs. WORD: 0.0433*	FLARE22 vs. WORD: 2.6896e-06*
Bones	CT-ORG vs. SAROS: 2.1364e-09*	CT-ORG vs. SAROS: 4.2888e-12*
Brain	CT-ORG vs. SAROS: 1.0	CT-ORG vs. SAROS: 1.0
Duodenum	FLARE22 vs. WORD: 1.3189e-09*	FLARE22 vs. WORD: 1.5321e-06*
Kidney Left	FLARE22 vs. WORD: 0.2095	FLARE22 vs. WORD: 0.0042*
Kidney Right	FLARE22 vs. WORD: 1.0	FLARE22 vs. WORD: 0.8368
Kidneys	CT-ORG vs. FLARE22: 1.7019e-06* CT-ORG vs. WORD: 3.6064e-10* FLARE22 vs. WORD: 1.0	CT-ORG vs. FLARE22: 0.0050* CT-ORG vs. WORD: 2.5901e-09* FLARE22 vs. WORD: 0.1195
Liver	CT-ORG vs. FLARE22: 1.0 CT-ORG vs. WORD: 1.0 FLARE22 vs. WORD: 1.0	CT-ORG vs. FLARE22: 2.4277e-05* CT-ORG vs. WORD: 0.0029* FLARE22 vs. WORD: 1.0
Lung Left	LCTSC vs. LUNA16: 1.0141e-05*	LCTSC vs. LUNA16: 6.1510e-06*
Lung Right	LCTSC vs. LUNA16: 1.9292e-05*	LCTSC vs. LUNA16: 1.3627e-08*
Lungs	CT-ORG vs. LCTSC: 0.0020* CT-ORG vs. LUNA16: 1.0 LCTSC vs. LUNA16: 2.2457e-06*	CT-ORG vs. LCTSC: 3.8623e-08* CT-ORG vs. LUNA16: 1.0 LCTSC vs. LUNA16: 1.1547e-06*
Pancreas	FLARE22 vs. WORD: 0.0006*	FLARE22 vs. WORD: 1.0
Pericardium	LCTSC vs. SAROS: 1.1399e-23*	LCTSC vs. SAROS: 1.5610e-27*
Spinal Cord	LCTSC vs. SAROS: 0.5081	LCTSC vs. SAROS: 1.0
Spleen	FLARE22 vs. WORD: 0.0001*	FLARE22 vs. WORD: 1.0
Stomach	FLARE22 vs. WORD: 3.3810e-06*	FLARE22 vs. WORD: 2.4462e-09*
Urinary Bladder	CT-ORG vs. WORD: 0.1782	CT-ORG vs. WORD: 5.6032e-06*

## C Implementation Details

To evaluate the model’s performance during training, a different Dice score formulation was devised. This approach uses the tree structure to create an encoding for each node, thereby eliminating the need to merge masks for evaluation purposes. The standard definition of Dice score can be computed using true positives (TP), false positives (FP), and false negatives (FN):

$$\text{Dice} = \frac{2 \cdot \text{TP}}{\text{TP} + \text{FP} + \text{FN}}.$$

Let  $y_c$  and  $\hat{y}_c$  be binary vectors representing the ground truth and the prediction for a specific class  $c$ . Then TP, FP, and FN can be computed for the same class  $c$  using simple logical operations such as a logical and ( $\wedge$ ) and logical not ( $\neg$ )

and by computing the bit summation over each voxel  $v$  in the voxels set  $V$ :

$$\begin{aligned} \text{TP}_c &= \sum_{v \in V} \hat{y}_c^{(v)} \wedge y_c^{(v)} \\ \text{FP}_c &= \sum_{v \in V} \hat{y}_c^{(v)} \wedge \neg y_c^{(v)} \\ \text{FN}_c &= \sum_{v \in V} \neg \hat{y}_c^{(v)} \wedge y_c^{(v)} \end{aligned}$$

To effectively assess the hierarchical relationships among classes, each class is assigned a bitwise encoding. The size of the encoding depends on the amount of bytes needed for uniquely encoding the node relationships. This means that the size of the encoding is  $N \times B$ , where  $B$  is the number of bytes. The bitwise encoding at position  $c$  of the matrix has size  $B$  and it is a signature that represents which nodes are traversed to get to node  $c$ , i.e., all the parents of the node. Additionally, a bitwise mask of size  $N \times B$  is also computed to mask the relevant bits of the encoding that correspond to the parents and the siblings of each node  $c$ . An example of the bitwise encoding and mask is shown in Figure 10. For bitwise signatures with no more than 64 bits of encoding, native data types from the numpy package<sup>57</sup> can be employed. In the other cases, the encoding can be split into individual bytes, and it requires an additional boolean logical and reduction operation to check for a binary match.

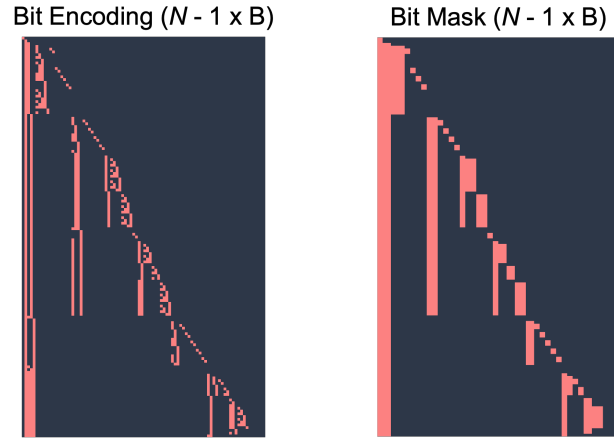


Figure 10: **Bitwise representation of the class hierarchy.** Both the bitwise encoding and the bitwise mask have size  $N \times B$ , representing the number of classes ( $N$ ) and the number of bytes ( $B$ ) needed to uniquely identify each node.

Using these two matrices, it is possible to compute the Dice for voxel  $v$  and class  $c$  by converting the ground truth ( $y$ ) and the prediction ( $\hat{y}$ ) to a binary representation that uses these encodings. Let  $v$  be a voxel of the ground truth  $y$  or of the prediction  $\hat{y}$ , and let  $c$  be the class for which the Dice is computed. To compute the binary representation  $\text{bin}(v, c)$ , the voxel  $v$  is first converted to its bit encoding, and then it is masked using the bitwise mask of class  $c$ :  $\text{bin}(v, c) = \text{encoding}(v) \wedge \text{mask}(c)$ . The result is a binary representation of the hierarchical affiliation of the voxel  $v$  to the class  $c$ . In practice, this is done for a set of voxels  $V$  at the same time, resulting in a two-dimensional array of binary representations of each voxel  $v \in V$ . The binary representation is then compared to the binary encoding  $\text{encoding}(c)$  of class  $c$  with an equality operator (equals):

$$\text{equals}(x, y) = \begin{cases} 1 & \text{if } x = y \\ 0 & \text{otherwise} \end{cases},$$

and the ground truth and the prediction are redefined as:

$$\begin{aligned} y'_c &= \text{equals}(\text{bin}(y_c, c), \text{encoding}(c)), \\ \hat{y}'_c &= \text{equals}(\text{bin}(\hat{y}_c, c), \text{encoding}(c)). \end{aligned}$$

Now,  $y'_c$  and  $\hat{y}'_c$  can be used to compute the Dice score with the true positive, false negative, and false positive formulas shown above.